Additive Manufacturing of ODS Steels Using Powder Feedstock Atomized with Elemental Yttrium

Seongun Yang [a,b], Donghua Xu [a], Dongqing Yan[a,b], Marc Albert [c], and Somayeh Pasebani [a,b, 1]

[a] School of Mechanical, Industrial, and Manufacturing Engineering, Oregon State University, Corvallis, OR, 97330

[b] Advanced Technology and Manufacturing Institute (ATAMI), Corvallis, OR 97330

[c] Advanced Nuclear Technology, Electric Power Research Institute, Charlotte, NC, 28262

Abstract

This study investigates the microstructure and mechanical properties of an austenitic ODS steel produced by the Laser Directed Energy Deposition (LDED) process using powder feedstock atomized with elemental yttrium. The Microstructure of the samples was characterized by electron microscopy, and mechanical properties were measured using a tensile test and nanoindentation. Further, the thermal stability of the LDED-produced ODS steels were evaluated. As-printed samples showed a cellular structure with Si-Mn-Y-O-enriched nanoparticles that were found to be amorphous. After 100 hours at 1000°C in an argon atmosphere, a partially recrystallized microstructure with a decrease in the number density of Y-O-enriched nanoparticles with crystalline structure was revealed. The as-printed (600 W, 600 mm/min) samples exhibited an ultimate tensile strength of 774 MPa and an elongation at a break of 22%. A lower ultimate tensile strength of 592 MPa and higher elongation of 42% was measured after 100 hours at 1000°C.

Keywords: Laser Directed Energy Deposition, oxide dispersion strengthened alloy, 316L stainless steel

Introduction

Oxide dispersion strengthened (ODS) alloys have garnered significant attention as potential game-changers in advanced reactor technology due to their fine distribution of nano-sized oxide particles embedded in either a ferritic or austenitic matrix [1]. These nanoparticles effectively impede grain growth and immobilize dislocations, resulting in enhanced strength, even at elevated temperatures [3]. Moreover, the cluster-matrix interfaces of ODS alloys can absorb point defects generated during irradiation, thereby reducing radiation-induced swelling [4]. Despite the advantageous high-temperature properties, thermal stability, and resistance to neutron radiation damage of ODS steels, they are not yet commercially available or widely utilized. This is primarily due to the complexities and costs associated with conventional ODS manufacturing methods [4]. While alternative manufacturing techniques, such as spark plasma sintering (SPS) [3, 4], have been explored to produce ODS alloys, they offer limited scalability. The poor fusion weldability of ODS steels has also limited their application [5]. Furthermore, the solid-state friction stir welding process for ODS steels remains suboptimal due to challenges like loss of mechanical properties in the plasticized zone, abnormal grain growth, potential coarsening, and the redistribution of Y-based nanoparticles [6].

One of the most widely used AM techniques for creating ODS alloys is laser directed energy deposition (LDED) [1]. In the LDED process, metal wires or powders are deposited onto a substrate to form solid structures. This method is particularly advantageous for producing large components and for repairing and restoring worn or damaged parts. Traditional methods for producing ODS alloys often involve ball milling. However, the use of gas-atomized powder containing elemental yttrium as a feedstock in LDED could potentially eliminate the need for ball milling. Wilms et al. [11] utilized metallic powder materials in an Ar-atomized state to explore the feasibility of manufacturing ODS composite materials via the DED process. Conveying nanometer-sized powder materials through conventional powder feeding systems is challenging due to the extensive agglomeration caused by electronic forces [11]. The study also employed mechanical alloying to produce the powder compound using grinding balls and milling containers. As a result, the powder compound consisted of metallic particles surrounded

by nanometer-scaled Y2O3 particles. Additionally, the study's findings indicated only minor deformation of the metallic particles during the milling process. Consequently, the study concluded that the powder compound was suitable for the powder feed system [11].

Sridharan et al. investigated the internal oxidation of 316L containing Y during the LDED process using gas-atomized powder. They compared results from parts manufactured in both reactive and inert atmospheres [14]. The mechanical properties of the samples were evaluated at room temperature and elevated temperatures, and these were compared with existing literature on wrought ODS alloys [15]. While the ultimate tensile strengths were found to be comparable, the deterioration in yield strength with increasing temperature was more pronounced in the AM-fabricated ODS material. Similarly, Miao et al. [12] determined that 316 steel exhibits both mechanical strength and radiation tolerance. However, the LDED-manufactured 316L+Y using gas-atomized powder showed greater ductility than all wrought 316L ODS alloys [7].

Saeidi et al. [8] and Wang et al. [13] demonstrated that oxide dispersion can be achieved during the LPBF of austenitic stainless steels, resulting in enhanced tensile properties at room temperature. However, the oxides identified were predominantly amorphous SiO2 and exhibited an incoherent and sharp interface with the matrix [8, 10]. Additionally, Ghayoor et al. [9] posited that ODS is a crucial approach for strengthening steel alloys. According to their study, ODS involves dispersing yttrium oxide nanoparticles within a metal matrix. This research also revealed that using selective laser melting (SLM) to fabricate ODS can aid in refining microstructures. Consequently, the study concluded that non-uniform layering and a lack of fusion were responsible for the differences between SLM 304L+5 wt. % and SLM 304L.

this study assesses the feasibility of manufacturing a 316L ODS alloy powder made through gas atomization. Its novelty lies in evaluating the mechanical properties of the fabricated samples and using powder-fed laser-directed energy deposition to make a 316L ODS alloy. Therefore, the primary focus of this study is to analyze the printability and mechanical properties of the 316L ODS alloy produced through LDED. Researchers must establish a correlation between processing parameters, and the resulting mechanical properties. The study utilized 316L yttrium oxide ODS powder as the feedstock to generate samples for assessment. The density, microstructure, and mechanical properties were evaluated to determine the optimal LDED processing parameters for the 316L yttrium oxide ODS. The impact of process parameters and post-process heat treatment on the density, microstructure, and mechanical properties were also examined. Hence, this study is unique as it comprehensively analyzes the manufacturing, mechanical properties, and impact of processes involved in producing a 316L ODS alloy powder.

Experimental Procedure

1. Preparation of Feedstock and Laser Directed Energy Deposition Process

Gas-atomized 316L stainless steel powder, containing 0.14 wt% yttrium oxide and henceforth referred to as 316LY, was sourced from Sandvik. The chemical composition of the feedstock powder is detailed in Table 1. The particle size distribution (PSD) of the powder was assessed using a Malvern Analytical particle analyzer (Mastersizer 3000).

Table 1. The chemical composition of powder according to Sandvik's datasheet

Element (wt.%)	Cr	Ni	Mo	Si	Mn	Y	O	C	P	S	Fe
316L+2Si+0.14Y	17.50	10.30	2.40	1.93	1.61	0.14	0.07	0.019	0.02	0.01	Bal.

For the fabrication of coupons meant for density and microstructure characterization (with dimensions of 20×20 mm), a Meltio M450 powder-wire LDED machine was employed. This machine is equipped with six CW diode lasers, each having a power of 200W and a wavelength of 976 nm. Tensile specimens were also fabricated in compliance with ASTM E8 standards. The build plate used in this study was crafted from stainless steel. The lasers were strategically positioned circumferentially/coaxially at the head, creating a hexagonal pattern on the

substrate with a working distance of 6 mm. A rotating grooved disk powder feeder was employed to ensure the consistent feeding of the powder feedstock into the melt pool. Argon, boasting a purity level of 99.99%, served as both the shield gas and the powder carrier. To mitigate oxidation, the oxygen concentration within the build chamber was meticulously maintained between 0 and 1%. The LDED parameters, which are elaborated upon in Table 2, were fine-tuned to achieve a relative density exceeding 99% and to prevent the occurrence of micro/macro defects.

Table 2. Optimized LDED process parameters used for this study

Process Parameter	Values used in this study
Laser Power (W)	600, 700, 800
Scanning speed (mm/min)	600
Powder feed rate (g/min)	1
Contact tip to work-piece distance (mm)	6
Laser spot size (mm)	0.8
Overlap distance (mm)	0.56 mm
Layer height (mm)	0.2

2. Microstructure characterization

The density of the LDED-produced 316LY samples was determined using the Archimedes method. Metallographic specimens were prepared following standard grinding and polishing procedures. Subsequently, they were electroetched in a solution comprising 10 wt.% oxalic acid and 90 wt.% deionized water, with an application of 15 V DC for 15 seconds. The microstructure of the samples was meticulously examined using optical microscopy (Zeiss, Axiotron), scanning electron microscopy (FEI Quanta 3D SEM), and electron dispersive X-ray spectroscopy (EDS).

3. Mechanical properties and microhardness

The microhardness of the LDED 316LY specimens was ascertained using a Leco Microhardness Tester (M-400A) with an applied load of 500 g. The average microhardness value was derived from at least 10 random indentations made on the cross-section perpendicular to the build direction.
For evaluating the mechanical properties at various testing temperatures, three dog bone specimens were crafted using wire electrical discharge machining (w-EDM) from rectangular blocks. These dog bones were designed in compliance with the ASTM E8 standard, featuring a gauge width of 6 mm, a thickness of 1.6 mm, and a gauge length of 32 mm. Notably, the test direction of the dog bones was set perpendicular to the build direction. Tensile tests were conducted on an Instron 5969 machine at room temperature, maintaining a strain rate of 10^{-3} s^{-1}.

4. Thermal stability

As-printed tensile specimens, accompanied by a small piece of pure Zr (serving as an oxygen getter), were sealed inside evacuated quartz tubes filled with 99.999% Ar, as depicted in Figure 1. These quartz tubes were subsequently placed in a Carbolite RHF chamber furnace. The samples underwent a heat treatment cycle at 1000°C for 100 hours, with both a heating and cooling rate set at 3.0°C/min.

Figure 1. An evacuated quartz tube with LDED 316Y tensile specimen and Zr (as oxygen absorber) subjected to thermal stability test

Results and Discussion

1. Powder Characterization

Figures 2a and 2b show the morphology of the 316LY powder, which consists of spherical particles. Finer satellite particles are observed attached to the larger ones, with a D50 measurement of 73.9 μm. The chemical composition of the powder's exterior surface, as depicted in Figure 2b, was analyzed using EDS. The EDS spot analysis results, presented in Figure 2c, confirmed the presence of elemental Y on the surface of the 316L powder.
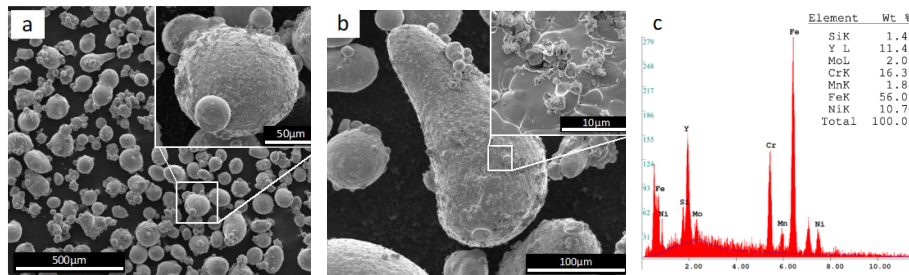

Figure 2. (a) SEM micrograph showing the morphology of 316LY feedstock powder, (b) higher magnification of 316LY powder, the inset shows the fragmentized yttria nanoparticles covering the surface of a 316L particle, and (c) EDS spot analysis on the fragmentized yttria nanoparticles shown in (b)

The particle shape, size, surface morphology, and flowability significantly influence the density of parts produced via the LDED process [16]. Consequently, powder flowability is a paramount consideration in the fabrication of components using the LDED technique. The Hausner ratio serves as a metric for powder flowability and is a dependable indicator of cohesion [17]. The physical attributes of the powder feedstock, including PSD, apparent density (AD), tap density (TD), and Hausner ratio measurements, are depicted in Figure 3 and detailed in Table 3, respectively. The Hausner ratio is defined as the quotient of tap density (ρ_T) to apparent density (ρ_A) and can be determined using the subsequent equation [18]:

$$H = \frac{\rho_T}{\rho_A} \quad (1)$$

Table 3. Physical properties of 316LY feedstock powder

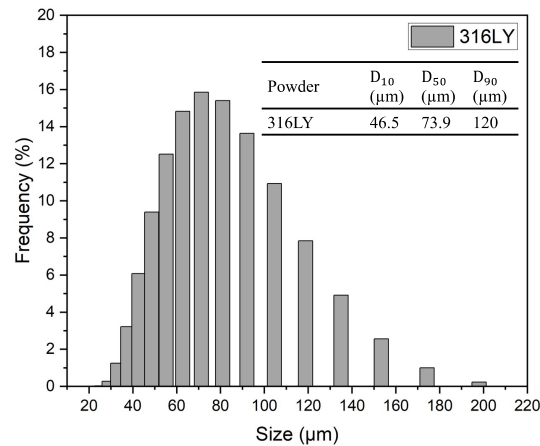| Powder	Apparent Density (g/cm³)	Tap density (g/cm³)	Hausner ratio
316L+2Si+0.3Y	3.945 ± 0.010	4.436 ± 0.041	1.124

Figure 3. A Malvern PSD histogram of 316LY feedstock powder

2.   Density of LDED 316LY ODS Samples

Relative density was determined by Archimedes' principle the method. A rule of mixture was applied to the nominal composition of 316LY and used as a bench mark for full density. Figure 4 shows the relative density values for the LDED-produced samples. The relative density of as-printed samples at 600 W was found to be 97.75±0.26%, which increased to 98.44±0.64% after thermal stability test. In contrast, the as-printed samples at 700 W showed an initial relative density of 99.02±0.35%. However, after heat treatment, this density reduced to 98.48±0.12%. Interestingly, despite the initial density differences stemming from different laser power settings, both conditions displayed comparable trends after heat treatment.
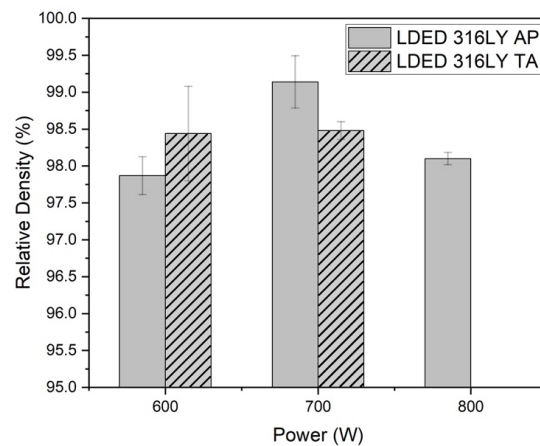

Figure 4. Relative densities of 316L+0.14Y LDED as-printed samples

The observed increase in porosity after heat treatment at 700 W could be attributed to the higher initial energy input during the additive manufacturing process, potentially leading to more pronounced residual stresses or structural defects that become exacerbated during heat treatment. The comparable final relative densities for both cases after heat treatment imply that the heat treatment process tends to converge towards a specific density, regardless of the initial laser power employed in the Directed Energy Deposition (DED) process.

3.   Microhardness of LDED 316LY ODS samples

Figure 5 shows the microhardness values for the as-printed samples (600W, 700W, 800W) and those post thermal stability test. As depicted in Figure 2.5, microhardness values consistently decreased from 266±5 HV to 234±19 HV as the laser power increased from 600W to 800W. Following 100 hours at 1000°C, there was a significant drop in microhardness values (approximately 180 HV) for samples at laser powers of 600W and 700W. This decline in microhardness suggests that the heat treatment induced notable alterations in the microstructure, potentially encompassing grain growth and the emergence of voids or defects. This observation aligns with the previously noted decrease in relative density after heat treatment. After the thermal stability test, the 600W (180±12HV) and 700W (179±17 HV) samples displayed comparable hardness values, implying that their microstructural attributes and mechanical behaviors became more aligned, irrespective of their initial as-printed conditions.
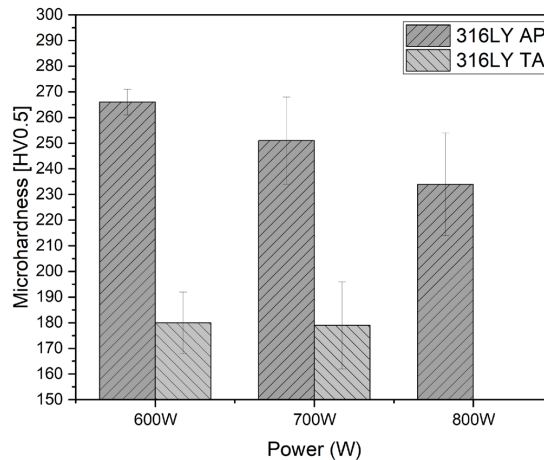

Figure 5. Microhardness values for 316LY produced at different laser power

4.   Microstructure Characterization

The melt pool boundaries, which were caused by the 90-degree rotational scanning strategy of the LDED process are shown in Figure 6. These boundaries correspond to the interfaces between individual laser beads indicating the laser scanning traces of every other layer, which extend in a perpendicular direction. The depth of the beads was approximately 250 µm, which was equivalent to the lamination thickness used in the LDED process.
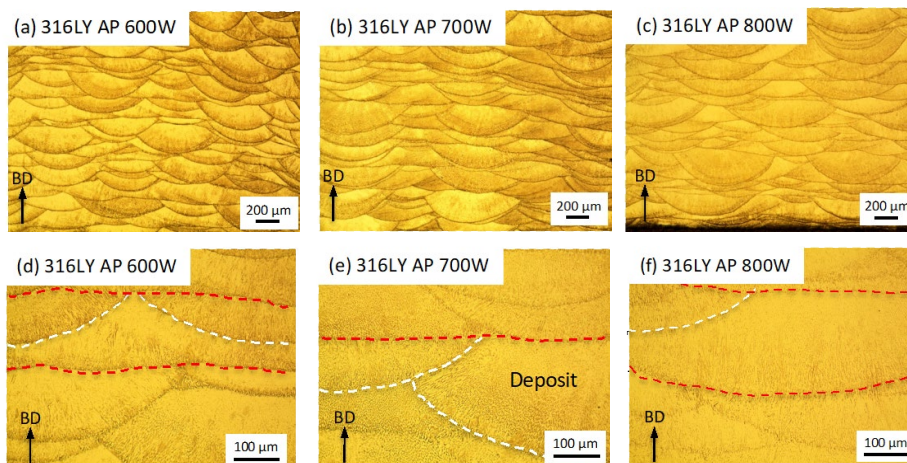

Figure 6. Optical micrographs of LDED produced 316LY As-printed: (a, d) 600 W, (b, e) 700 W and (c,f) 800 W

The optical micrographs shown in Figures 6a and 6c demonstrate the relationship between laser power and the depth and width of the melt pool. As laser power increased, more energy was absorbed by the powder, resulting in higher temperatures and longevity of the molten material leading to a deeper and wider melt pool. Figure 6a-f illustrate the cellular pattern microstructure formed due to the rapid solidification rate in laser-scanned regions, a general characteristic of LDED produced samples.
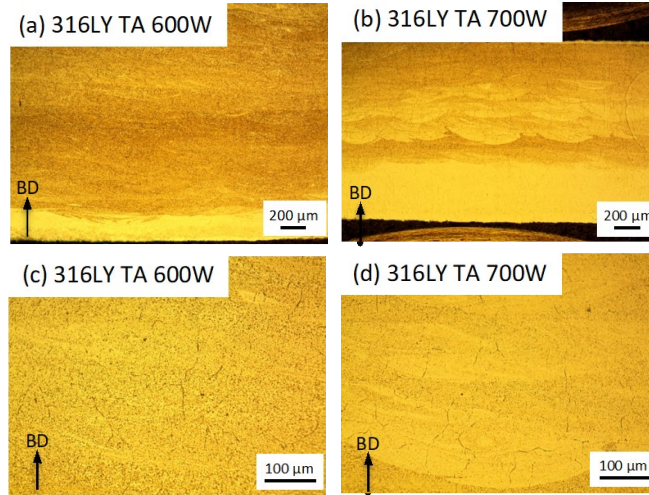

Figure 7. Optical micrographs of LDED produced 316LY Thermal aged: (a, c) 600 W and (b, d) 700 W

Figure 7 presents optical micrographs that demonstrate changes in the microstructure of 316LY steel resulting from LDED and undergoing a heat treatment at 1000°C for 100 hours. At 600 W and 700 W, the micrographs show similar results. Extended heat treatment causes the melt pool boundaries to disappear. The disappearance of these boundaries indicates significant homogenization of the microstructure, perhaps due to activated diffusive processes during the heat treatment.
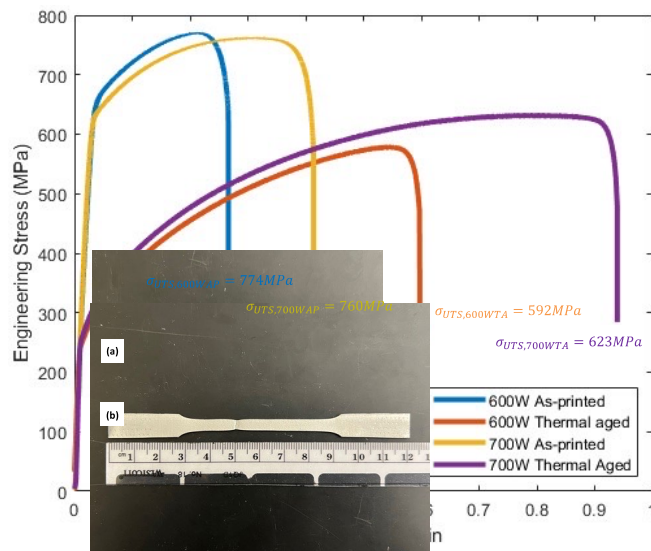
5. Mechanical behavior

Figure 8. Engineering stress-stain curves of as-printed and thermal aged according to laser power, (a) As-printed LDED 316LY ODS alloy at 700 W, and (b) after 100 hours at 1000℃

Figure 8 shows the room temperature stress-strain curve for the as-printed LDED produced 316LY ODS and after 100 hours at 1000oC. The results showed that the 600W-AP specimen exhibited the highest ultimate tensile strength of 774 MPa, with an elongation at a break of 22% at RT. The addition of oxide nanoparticles in the current study improved the ultimate tensile strength through a dispersion mechanism [19]. The sample 600W-TA exhibited a lower ultimate tensile strength of 592 MPa, with an elongation at a break of 42%. The thermally aged specimen 700W-TA showed an ultimate tensile strength of 623 MPa and an elongation of 67%. The tensile results are summarized in Table 4.

Table 4. Comparison between the mechanical properties of the samples produced in the work with different production processes.

	YS (MPa)	UTS (MPa)	ε_r(%)	Ref.
LDED 600W-AP	611±7.9	774±3.7	22±0.2	Current work
LDED 600W-TA	230±5.2	592±19.3	42±1.4	Current work
LDED 700W-AP	604±13.8	760±6.7	32±2.2	Current work
LDED 700W-TA	250±3.6	623±13.2	67±3.8	Current work
SLM 316L SS	495 - 500	610 - 620	38 - 48	[20]
LPBF 304L ODS	575±8	700±13	32±5	[23]
Wrought 316L SS	255 - 310	450	30	[21]
As Cast 316L SS	262	552	55	[22]

The fracture surfaces of the specimens labeled 700W-AP and 700W-TA are depicted in Figure 9. Both samples displayed dimples, indicative of a ductile mode of failure. For the 700W-AP specimen, the dimple sizes ranged between 1 and 2.2 μm, while for the 700W-TA, they were between 1 and 2.5 μm. Within these larger dimples, one can observe smaller particles, roughly 0.33 μm across. The presence of these particles inside the dimples hints at possible sites where cracks might initiate, potentially leading to the material's eventual breakdown.
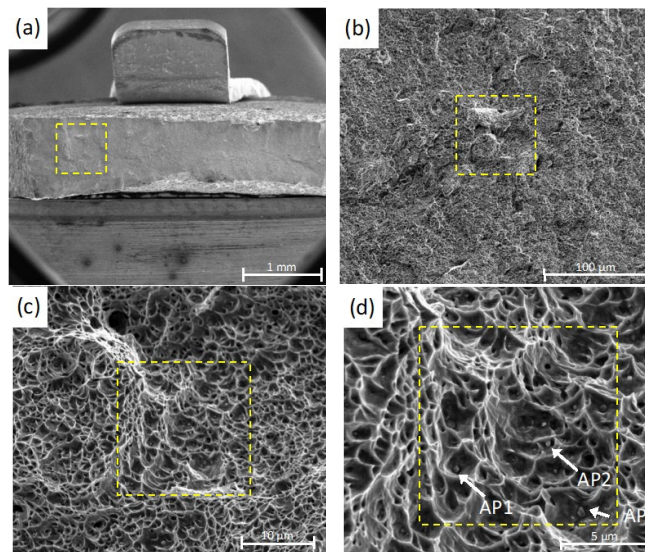
(a) As-printed LDED 316LY ODS alloy (700 W)
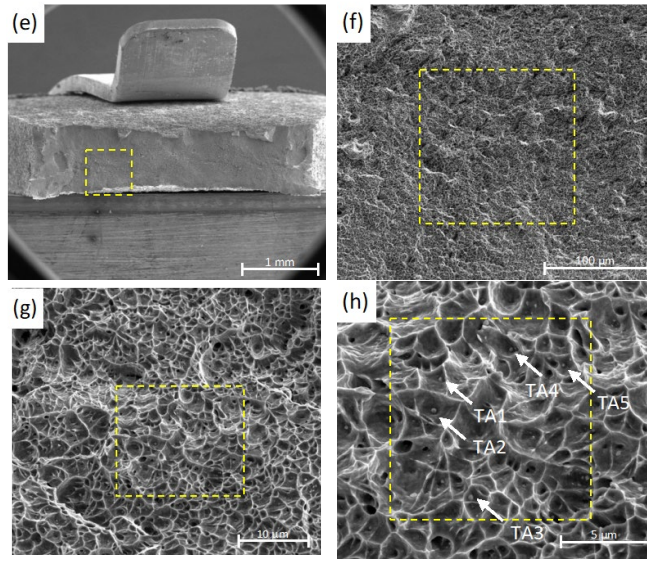
(b) LDED 316LY ODS alloy after 100 hours at 1000℃ (700W)

Figure 9. SEM micrograph showing the fracture surface of LDED 316LY ODS alloy and dimples, Y-riched nanoparticles with corresponding EDS chemical analysis (pointed by arrow), (a-d) 700W as-printed LDED 316LY ODS alloy, and (e-h) 700W LDED 316LY ODS alloy at 1000℃ for 100 hours.

EDS analysis was conducted on these particles, which confirmed the Y-rich composition in Table 5. This finding could suggest that the oxide nanoparticles contributing to the dispersion-strengthening mechanism are Yttrium-based. The persistence of Y-rich nanoparticles after thermal aging, and their association with potential crack initiation sites, suggests a complex interaction between the nanoparticle dispersion, grain structure, and mechanical properties.

Table 5. Chemical analysis by EDS point analysis performed on the dimples of LDED 316LY 700W as-printed and thermal aged

Elements (wt.%)		Fe	Ni	Cr	Mn	Y	Si	O	Mo
LDED 316LY 700W As-printed	AP 1	42.54	6.47	6.69	0.00	35.64	0.67	6.27	1.72
	AP 2	59.71	11.27	12.86	0.57	10.69	1.65	1.42	1.84
	AP 3	48.49	8.63	8.96	0.00	25.50	1.15	5.81	1.46
LDED 316LY 700W Thermal Aged	TA 1	54.04	8.55	11.28	0.00	20.76	1.50	1.91	1.96
	TA 2	38.76	5.12	26.24	0.00	21.43	0.29	2.09	6.07
	TA 3	38.02	5.21	7.12	0.89	36.82	0.83	9.14	1.97
	TA 4	37.89	3.74	38.27	1.62	13.59	1.08	1.43	2.38
	TA 5	48.30	7.66	11.25	0.89	22.93	1.04	5.54	2.39

Summary and Conclusion

The LDED technique has been explored for its capability to produce ODS alloys, with particular attention to how yttrium oxide nanoparticles, formed through internal oxidation reactions in the chamber, influence the microstructure and strength of 316LY alloy samples; the findings offer valuable understanding into the relationship between these nanoparticles and the microstructure and mechanical properties of the alloy samples.

The key findings are summarized below:

1) The microhardness of the as-printed specimens was found to be between 234 and 266 HV for laser power of 800W and 600W, respectively. However, heat treatment caused the hardness values of the LDED fabricated 316LY stainless steel specimen to decrease to 180 HV for a sample that was aged at 1000 °C for 100 hours.

2) The mechanical properties of the as-printed samples were also studied and found to be comparable to the thermally aged condition. For example, the as-printed samples exhibited an ultimate tensile strength of 774 MPa and an elongation at a break of 22% at room temperature for sample 600W-AP. However, the thermal aged samples had a lower ultimate tensile strength of 592 MPa and 623 MPa, along with increased elongations of 42% and 67% at 600 W and 700 W, respectively.

3) The fracture surfaces of the 316LY 700W samples, both as-printed and thermally aged, exhibited ductile failure modes, as evidenced by the presence of dimples. Y-rich nanoparticles were identified within these dimples, suggesting potential crack initiation sites, which indicates their role in the dispersion-strengthening mechanism.

Acknowledgment

References:

1. Allen, T., Busby, J., Meyer, M., and Petti, D., Materials challenges for nuclear systems. Materials Today, 2010. 13(12): p. 14-23.

2. Ghayoor, M., Lee, K., He, Y., Chang, C.-h., Paul, B.K., and Pasebani, S., Selective laser melting of austenitic oxide dispersion strengthened steel: Processing, microstructural evolution, and strengthening mechanisms. Materials Science and Engineering: A, 2020: p. 139532.

3. Pasebani, S., Dutt, A.K., Burns, J., Charit, I., and Mishra, R.S., Oxide dispersion strengthened nickel based alloys via spark plasma sintering. Materials Science and Engineering: A, 2015. 630: p. 155-169.

4. Pasebani, S., Charit, I., Wu, Y., Burns, J., Allahar, K.N., Butt, D.P., Cole, J.I., and Alsagabi, S.F., Lanthana-bearing nanostructured ferritic steels via spark plasma sintering. Journal of Nuclear Materials, 2016. 470: p. 297-306.

5. Yu, Z., Feng, Z., Hoelzer, D., Tan, L., and Sokolov, M.A., Friction stir welding of ODS and RAFM steels. Metallurgical and Materials Transactions E, 2015. 2(3): p. 164-172.

6. Noh, S., Kasada, R., Kimura, A., Park, S.H.C., and Hirano, S., Microstructure and mechanical properties of friction stir processed ODS ferritic steels. Journal of Nuclear Materials, 2011. 417(1-3): p. 245-248.

7. Imandoust A, Zarei-Hanzaki A, Heshmati-Manesh S, Momeni S, and Changizian P 2014 Effects of ferrite volume fraction on the tensile deformation characteristics of dual phase twinning induced plasticity steel, Materials & Design 53 99-105

8. Saeidi, K., Kvetková, L., Lofaj, F., and Shen, Z., Austenitic stainless steel strengthened by the in situ formation of oxide nano inclusions. RSC Advances, 2015. 5(27): p. 20747-20750.

9. Ghayoor, M., Mirzababaei, S., Lee, K., He, Y., Chang, C.-h., Paul, B.K., and Pasebani, S. Strengthening of 304L Stainless Steel by Addition of Yttrium Oxide and Grain Refinement during Selective Laser Melting. in Annual International Solid Freeform Fabrication Symposium: Austin, TX, USA. 2019.

10. Y. Xu, Z. Zhou, M. Li, and P. He, Fabrication and characterization of ODS austenitic steels. Journal of Nuclear Materials. 417 (1-3) (2011) p. 283-285.

11. Wilms, Markus B., Norbert Pirch, and Bilal Gökce. "Manufacturing oxide-dispersion-strengthened steels using the advanced directed energy deposition process of high-speed laser cladding." Progress in Additive Manufacturing (2022): 1-9.

12. Miao, Y., Mo, K., Zhou, Z., Liu, X., Lan, K.-C., Zhang, G., Miller, M.K., Powers, K.A., Mei, Z.-G., and Park, J.-S., On the microstructure and strengthening mechanism in oxide dispersion-strengthened 316 steel: A coordinated electron microscopy, atom probe tomography and in situ synchrotron tensile investigation. Materials Science and Engineering: A, 2015. 639: p. 585-596.

13. Wang, Y.M., Voisin, T., McKeown, J.T., Ye, J., Calta, N.P., Li, Z., Zeng, Z., Zhang, Y., Chen, W., and Roehling, T.T., Additively manufactured hierarchical stainless steels with high strength and ductility. Nature materials, 2018. 17(1): p. 63-71.

14. Sridharan, Niyanth, Dryepondt, Sebastien N., and Field, Kevin G.. Investigation of laser direct energy deposition for production of ODS alloys. United States: N. p., 2018. Web. doi:10.2172/1658016.

15. Bouche G, Bechade J, Mathon M, Allais L, Gourgues A, and Naze L 2000 Texture of welded joints of 316L stainless steel, multi-scale orientation analysis of a weld metal deposit, Journal of nuclear materials 277 91-8

16. Li SH, Zhao Y, Kumar P, Ramamurty U. Effect of initial dislocation density on the plastic deformation response of 316L stainless steel manufactured by directed energy deposition. Materials Science and Engineering: A. 2022 Aug 23;851:143591.

17. S. Sivasankaran, K. Sivaprasad, R. Narayanasamy, V.K. Iyer, An investigation on flowability and compressibility of AA 6061100 − x-x wt.% TiO2 micro and nanocomposite powder prepared by blending and mechanical alloying, Powder Technol. 201 (1) (2010) 70–82

18. Yan Z, Zou K, Cheng M, Zhou Z, Song L. Revealing relationships between heterogeneous microstructure and strengthening mechanism of austenitic stainless steels fabricated by directed energy deposition (DED). Journal of Materials Research and Technology. 2021 Nov 1;15:582-94.

19. Wilms MB, Rittinghaus SK, Goßling M, Gökce B. Additive manufacturing of oxide-dispersion strengthened alloys: Materials, synthesis, and manufacturing. Progress in Materials Science. 2022 Nov 26:101049.

20. R. Casati, J. Lemke, M. Vedani, Microstructure and Fracture Behavior of 316L Austenitic Stainless Steel Produced by Selective Laser Melting, J. Mater. Sci. Technol. 32 (2016) 738–744.

21. Yadollahi, N. Shamsaei, S.M. Thompson, D.W. Seely, Effects of process time interval and heat treatment on the mechanical and microstructural properties of direct laser deposited 316L stainless steel, Mater. Sci. Eng. A. 644 (2015) 171–183.

22. T. Kurzynowski, K. Gruber, W. Stopyra, B. Kuźnicka, E. Chlebus, Correlation between process parameters, microstructure and properties of 316 L stainless steel processed by selective laser melting, Mater. Sci. Eng. A. 718 (2018) 64–73.

23. M. Ghayoor, K. Lee and Y. He, Microstructure and mechanical properties of selective laser melted 304L ODS alloy, Journal of Materials Research and Technology, vol. 13, pp. 1-10, 2021.